



Cite this: *Nanoscale*, 2021, **13**, 16932

Photoelectrochemical H₂ evolution on WO₃/BiVO₄ enabled by single-crystalline TiO₂ overlayer modulations†

Eunoak Park,^a Santosh S. Patil,^a Hyeonkwon Lee,^b Vijay S. Kumbhar*^c and Kiyoung Lee  ^{*a}

Tungsten oxide/bismuth vanadate (WO₃/BiVO₄) has emerged as a promising photoanode material for photoelectrochemical (PEC) water splitting owing to its facilitated charge separation state differing significantly from single phase materials. Practical implementation of WO₃/BiVO₄ is often limited by poor stability arising from the leaching of V⁵⁺ from BiVO₄ during PEC operations. Herein, we demonstrate that the synthesis of a tungsten oxide/bismuth vanadate/titanium oxide (WO₃/BiVO₄/TiO₂) heterostructure onto a fluorine-doped tin oxide-coated glass substrate through a combined simple hydrothermal-spin coating strategy will advance PEC performance while slowing water oxidation kinetics and improving photostability. We show that surface postmodification with a nanometer-thick layer of (1 0 1) monofacet-selective single-crystalline TiO₂ provides stable photocurrent density, up to 1.04 mA cm⁻² at 1.23 V (compared to a reversible hydrogen electrode in 0.5 M Na₂SO₄), with excellent quantum efficiency (45% at 460 nm) and long-term photostability (24 h). Interestingly, crystalline TiO₂ activation layers behave differently from previous TiO₂ amorphous layers, blocking surface defects while improving corrosion resistance, photostability, and the electron transfer process. These results indicate a ≈2.5 times enhancement in photoelectrocatalytic activity related to referenced WO₃/BiVO₄ photoanodes, encouraging the use of single-crystalline TiO₂ modulations to develop a range of materials for PEC/photocatalytic applications.

Received 22nd July 2021,

Accepted 13th August 2021

DOI: 10.1039/d1nr04763a

rsc.li/nanoscale

Introduction

Converting solar energy into hydrogen (H₂) energy *via* photoelectrochemical water splitting is a cost effective and sustainable approach for mitigating overreliance on fossil fuels and global warming issues.^{1,2} As H₂ energy is renewable, it can be stored, transported, and even used in fuel cells to generate power and/or is an important feedstock in the chemical industry (*e.g.*, in the catalytic conversion of CO₂ into hydrocarbons, such as methanol, formic acid, methane, or ammonia synthesis).^{3–5} Photoelectrochemical (PEC) water splitting (H₂O → H₂ + 1/2 O₂) is based on photogenerated electron-hole pairs in a semiconductor that subsequently catalyze the oxidation

and reduction of a H₂O molecule into H₂ and O₂ fuels.⁶ However, the practical implementation of PEC cells remains hindered by stringent material challenges that simultaneously require (i) excellent light harvesting capability, (ii) long-term stability, and (iii) charge-carrier separation and transfer. Since Fujishima Honda's⁷ pioneering work on titanium dioxide (TiO₂) photocatalysts, various visible-light responsive metal oxides (such as tungsten oxide (WO₃), bismuth vanadate (BiVO₄), and iron(III) oxide (Fe₂O₃)) have been examined to absorb a major fraction of the solar spectrum and produce green H₂. However, those single materials are insufficient to deliver high solar-hydrogen-conversion efficiency for practical application.

A number of strategies have been developed by combining two or more semiconductors, co-catalysts for constructing heterostructures, integrated material designs, or composites that provide an opportunity to achieve multiple catalytic functionalities from different counterparts; these have enhanced PEC/photocatalytic performance and stability regarding water splitting and environmental remediation applications. For instance, a combination of WO₃ and BiVO₄ creates a type II heterojunction and enhances PEC performance,^{8,9} which

^aDepartment of Chemistry and Chemical Engineering, Inha University, 22212 Incheon, Republic of Korea. E-mail: kiyoung@inha.ac.kr

^bResearch Institute of Environmental Science & Technology, Kyungpook National University, 80 Daehak-ro, Buk-guDaegu, Republic of Korea

^cApplied Chemistry, Graduate School of Sciences and Technology for Innovation, Yamaguchi University, Japan. E-mail: vijay1712phy@gmail.com

† Electronic supplementary information (ESI) available. See DOI: 10.1039/d1nr04763a

mainly stems from the excellent transference of photogenerated electrons to produce a charge-separated state.^{10–12} Nonetheless, while $\text{WO}_3/\text{BiVO}_4$ is a relatively stable material, it often suffers from severe V^{5+} leaching out of the BiVO_4 core during photoelectrocatalytic operations.¹³

Postmodification of a $\text{WO}_3/\text{BiVO}_4$ heterojunction with a surface protecting promoter is indispensable to realize potentially high PEC performance with long-term durability. Previous efforts have mainly relied on building an additional passivation layer onto a $\text{WO}_3/\text{BiVO}_4$ semiconductor pair.^{14–17} For example, Khoomortezaei *et al.*¹⁴ reported tungsten oxide/bismuth vanadate/bismuth ferrite ($\text{WO}_3/\text{BiVO}_4/\text{BiFeO}_3$) heterojunctions with a layered coating of BiFeO_3 that lowered the overpotential and charge transfer resistance of the photoelectrode. Baek *et al.*¹¹ made a tin oxide/tungsten oxide/bismuth vanadate ($\text{SnO}_2/\text{WO}_3/\text{BiVO}_4$) triple-layer planar photoelectrode that exhibited superior photoconversion efficiency during water decomposition. Recently, Seo *et al.*¹⁸ added a photocatalytically inactive amorphous TiO_2 layer onto a $\text{WO}_3/\text{BiVO}_4$ electrode that reduced charge-carrier recombination by passivating the surfaces. Although previous studies have made remarkable developments, they used amorphous TiO_2 overlayers and met with little success in attaining sufficient stability. Simple solution-processed synthesis of crystalline TiO_2 can offer a means of creating intricately designed $\text{WO}_3/\text{BiVO}_4$ heterostructures that otherwise defy creation. We anticipate that depositing a nanometer-thick layer of single-crystalline TiO_2 onto $\text{WO}_3/\text{BiVO}_4$ may grant proficient catalytic operations with long-term durability.

Herein, we present the synthesis of a $\text{WO}_3/\text{BiVO}_4/\text{TiO}_2$ heterojunction using a simple hydrothermal-spin coating method. Postmodification with crystalline TiO_2 was accomplished and played a key role in blocking surface defects in BiVO_4 nanoparticles,¹⁹ leading to substantial improvements in electronic properties and photostability. The $\text{WO}_3/\text{BiVO}_4/\text{TiO}_2$

heterojunction showed the best photocurrent density of 1.04 mA cm^{-2} at 1.23 V when compared to a reversible hydrogen electrode (RHE), an incident photon-to-current conversion efficiency (IPCE) of 25% in response to visible light at 460 nm , and exceptionally high durability (24 h) in $0.5 \text{ M Na}_2\text{SO}_4$ at $1.23 \text{ V}_{\text{RHE}}$ under standard 1 sun illumination (100 mW cm^{-2}). According to gas chromatography analysis, the utmost H_2 evolution rate of $78.8 \text{ } \mu\text{L cm}^{-2}$ was achieved during PEC water splitting.

Results and discussion

The surface morphologies of WO_3 , $\text{WO}_3/\text{BiVO}_4$, and $\text{WO}_3/\text{BiVO}_4/\text{TiO}_2$ electrodes synthesized through a hydrothermal-spin coating method were evaluated with scanning electron microscopy (SEM) images (Fig. 1). The prepared WO_3 showed rough nanoplate shapes with relatively dense distributions ranging from nanometer to submicrometer scales (Fig. 1a). Interconnected nanoplates were grown nearly vertical to the fluorine-doped tin oxide (FTO) surface, creating several void spaces between them. The average length and thickness of the individual nanoplates were $\sim 400\text{--}600 \text{ nm}$ and $100\text{--}160 \text{ nm}$, respectively, as confirmed by the cross-section and top view SEM images (Fig. 1a and d). Fig. 1c and f depict the top and cross-section views of SEM images after the deposition of BiVO_4 nanoparticles (20 cycles) onto WO_3 via a spin coating method and subsequent air annealing at $500 \text{ }^\circ\text{C}$. While BiVO_4 nanoparticles with diameters $\sim 50\text{--}80 \text{ nm}$ were uniformly coated onto WO_3 nanoplate surfaces, overlayer thicknesses seemed irregular, indicating a possible overgrowth of BiVO_4 nanoparticles (Fig. S1b and c in the ESI†). A thin top layer of TiO_2 was formed onto the $\text{WO}_3/\text{BiVO}_4$ by spin coating a titanium butoxide ($\text{Ti}(\text{OCH}_2\text{CH}_2\text{CH}_2\text{CH}_3)_4$) solution and subsequent annealing at $500 \text{ }^\circ\text{C}$ for 1 h (Fig. 1c and f).



Eunoak Park

Eunoak Park received her B.S. degree from the Kyungpook National University, Republic of Korea in 2019. After that, she started her master's degree in Kyungpook National University and moved to Inha University, Republic of Korea in 2021. Her research interests are focused on anodization, synthesis of nano-structure materials with heterojunction, photoelectrochemistry, photocatalyst, water electrolysis (hydrogen evolution), and various other applications.



Santosh S. Patil

Dr Santosh S. Patil received his Ph.D. in Chemistry from Shivaji University, Kolhapur (India) in 2016. After that, he conducted his post-doctoral studies at Chonnam National University, POSTECH, Kyungpook National University and Inha University (S. Korea). His research interests are focused on the synthesis of nanostructured materials, thin films, and photocatalysts, structure–composition–property control and investigating the fundamental process of charge-carrier dynamics at the interface of these materials to increase the overall efficiency of operations particularly for catalysis, energy conversion (hydrogen generation), waste water treatment and various other applications.

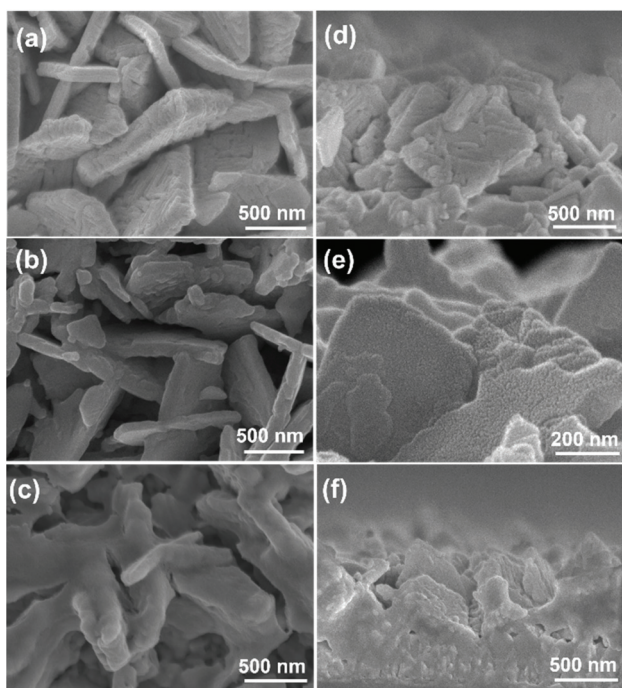


Fig. 1 (a–c) Top view and (d–f) cross-sectional FE-SEM images of WO_3 , $\text{WO}_3/\text{BiVO}_4$, and $\text{WO}_3/\text{BiVO}_4/\text{TiO}_2$, respectively.

Crystal structures were analyzed further by acquiring X-ray diffraction (XRD) patterns. Fig. 2a shows the prominent diffraction peaks at 23.0° , 23.5° , 24.3° , 28.7° , 34.0° , 41.6° , 49.9° , 55.7° , and 76.4° ; these can be assigned to the $(0\ 0\ 2)$, $(0\ 2\ 0)$, $(2\ 0\ 0)$, $(1\ 1\ 2)$, $(2\ 2\ 0)$, $(2\ 3\ 2)$, $(-2\ 4\ 1)$, $(4\ 0\ 2)$, and $(0\ 6\ 1)$ planes, respectively, representing monoclinic WO_3 (JCPDS #89-4921).



Hyeonkwon Lee

Hyeonkwon Lee fulfilled a bachelor's and master's degree at Kyungpook National University in South Korea where he studied electrocatalytic and capacitive properties of metal oxides. Subsequently, seeking to meet his scientific interests, he joined the University of Cologne in Germany. His current research topic is to find magnetic fields effect on the growth of metal oxides and their electrochemical properties.

4476).^{20,21} The $\text{WO}_3/\text{BiVO}_4$ heterojunction showed preservation of the WO_3 phase and Bragg diffractions at 18.8° , 28.9° , 30.4° , and 39.8° ; these correspond to the $(1\ 0\ 1)$, $(1\ 1\ 2)$, $(0\ 0\ 4)$, and $(2\ 1\ 1)$ planes, respectively, suggesting the generation of a monoclinic BiVO_4 form (JCPDS #75-1866).^{22,23} As illustrated in Fig. 2b (a magnified view of an XRD pattern), the one-cycle coated TiO_2 shows a Bragg peak at 25.3° , confirming the generation of $(1\ 0\ 1)$ selective single-crystalline anatase TiO_2 (JCPDS #89-4921) nanoparticles.^{24,25} The XRD pattern of a five-cycle spin coated TiO_2 (Fig. S3†) revealed a diffraction peak at 48.1° , implying the $(2\ 0\ 0)$ plane of anatase TiO_2 together with the heightened peak intensity of the $(1\ 0\ 1)$ crystal plane.

High-angle annular dark-field STEM (HAADF-STEM) was employed to investigate crystalline contacts between $\text{WO}_3/\text{BiVO}_4/\text{TiO}_2$ components. The area marked A in Fig. 3a illustrates a high-resolution transmission electron microscopy (TEM) image with measured lattice spacings of 0.263 nm and 0.164 nm ; this agrees well with the $(2\ 2\ 0)$ and $(4\ 0\ 2)$ planes of WO_3 . The selected area electron diffraction (SAED) pattern (Fig. 3d) confirms a polycrystalline nature, and the $(2\ 2\ 0)$ and $(4\ 0\ 2)$ planes correspond to monoclinic WO_3 . Fig. 3e (the area marked B in Fig. 3a) shows clear lattice fringes with lattice spacings of 0.308 nm and 0.349 nm that correspond with the $(1\ 1\ 2)$ and $(1\ 0\ 1)$ planes of monoclinic BiVO_4 and anatase TiO_2 , respectively. The corresponding SAED pattern (Fig. 3f) reveals that single-crystalline TiO_2 is oriented along the $(1\ 0\ 1)$ facet. Energy dispersive X-ray spectroscopy (EDS) elemental maps were acquired (Fig. 3b1–b5) to investigate the composition of $\text{WO}_3/\text{BiVO}_4/\text{TiO}_2$, demonstrating that five elements (W, O, Bi, V, and Ti) were uniformly distributed throughout the entire structure.



Vijay S. Kumbhar

Dr Vijay S. Kumbhar obtained his PhD investigating the supercapacitive properties of samarium based rare earth chalcogenides from Shivaji University, Kolhapur, India, in 2015. Then, he has a wide range of postdoctoral experience in energy storage at several materials science laboratories in South Korea. He has been associated with Professor Kiyoung Lee since 2018. He is a recipient of the National Postdoctoral Fellowship

from the Science and Engineering Research Board, India as well as the Japan Society for the Promotion of Science (JSPS), Japan. Dr Vijay has published about 40 research and review articles. His current research area mainly focusses on the formation of core-shell based materials for energy generation and storage such as electrocatalysis, photoelectrocatalysis, oxygen reduction reaction, and supercapacitors.

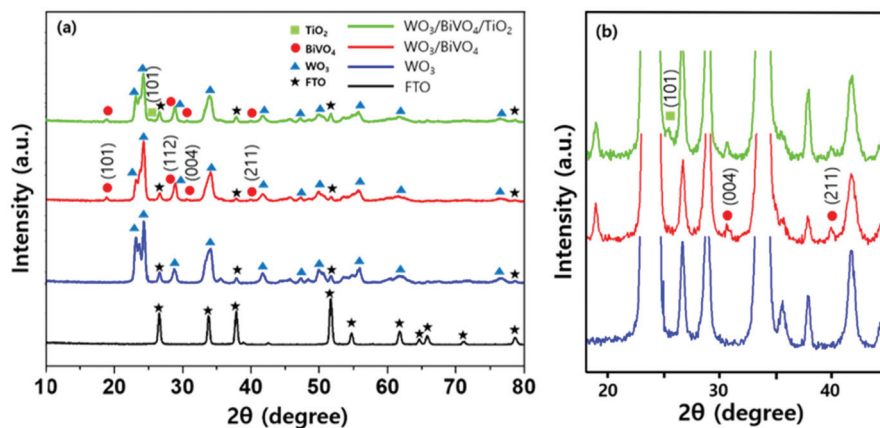


Fig. 2 XRD patterns of (a) FTO, WO_3 , $\text{WO}_3/\text{BiVO}_4$, and $\text{WO}_3/\text{BiVO}_4/\text{TiO}_2$ samples and (b) the corresponding magnified view.

X-ray photoelectron spectroscopy (XPS) was performed to verify chemical states and compositions. Fig. 4a depicts the survey spectra, confirming the presence of Ti, W, Bi, V, and O elements in the $\text{WO}_3/\text{BiVO}_4/\text{TiO}_2$ heterojunction. High-resolution XPS spectra of W 4f (Fig. 4b) show main peaks at binding energies of 35.9 and 38 eV, which can be attributed to the respective W 4f_{7/2} and W 4f_{5/2} states of the W^{6+} valence state.²⁶ Fig. 4c shows two peaks at binding energies of 159.6 and 164.8 eV, demonstrating that the respective Bi 4f_{7/2} and Bi 4f_{5/2} orbits exhibit a 3+ valence state in BiVO_4 .²⁷ The convoluted signals of V 2p_{3/2} and V 2p_{1/2} peaks (shown in Fig. 4d) at 517.1 and 524.6 eV, respectively, clearly reveal an oxidation state of V^{5+} in BiVO_4 .²⁸ The spin orbit coupling of Ti 2p_{3/2} and Ti 2p_{1/2} peaks (see Fig. 4e) showed binding energies of 459.4 and 465 eV, respectively, demonstrating the presence of TiO_2 with a valence state of Ti^{4+} .²⁹ The asymmetric peak of O 1s at \sim 530.7

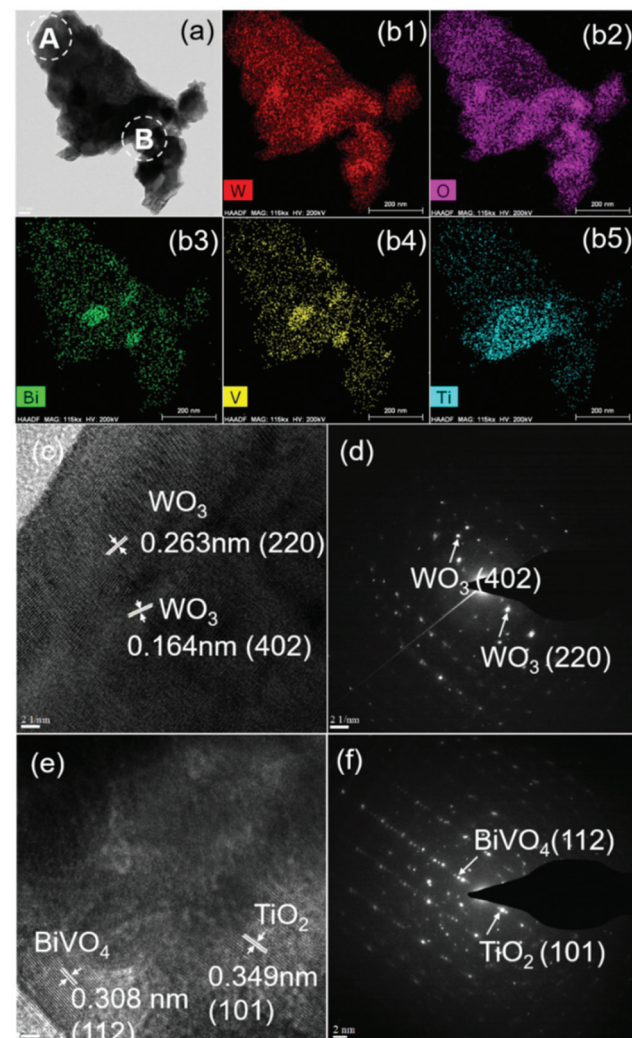


Fig. 3 (a) TEM image recorded in the HADDF mode of $\text{WO}_3/\text{BiVO}_4/\text{TiO}_2$; (b1–b5) corresponding elemental analysis by EDS mapping of W, O, Bi, V, and Ti levels; (c) HR-TEM images of $\text{WO}_3/\text{BiVO}_4/\text{TiO}_2$ for areas marked A in 3(a); (d) corresponding SAED pattern; (e) HR-TEM images of $\text{WO}_3/\text{BiVO}_4/\text{TiO}_2$ for areas marked B in 3(a); and (f) corresponding SAED pattern.



Kiyoung Lee

Kiyoung Lee studied Chemical Engineering at Inha University, Korea and obtained his Ph.D. from the University of Erlangen-Nuremberg, Germany in 2013. From 2013 to 2015, he worked at the University of Erlangen-Nuremberg, Germany and the University of California, Riverside, US as a postdoctoral researcher. From 2016 to 2021, he was an assistant and associate professor at the School of Nano & Materials Science and

Engineering of Kyungpook National University, Korea. Since 2021, he has been an associate professor at the Department of Chemical Engineering, Inha University, Korea. His current research interests include functional nanomaterial synthesis by electrochemical methods and their use in energy conversion and storage devices.

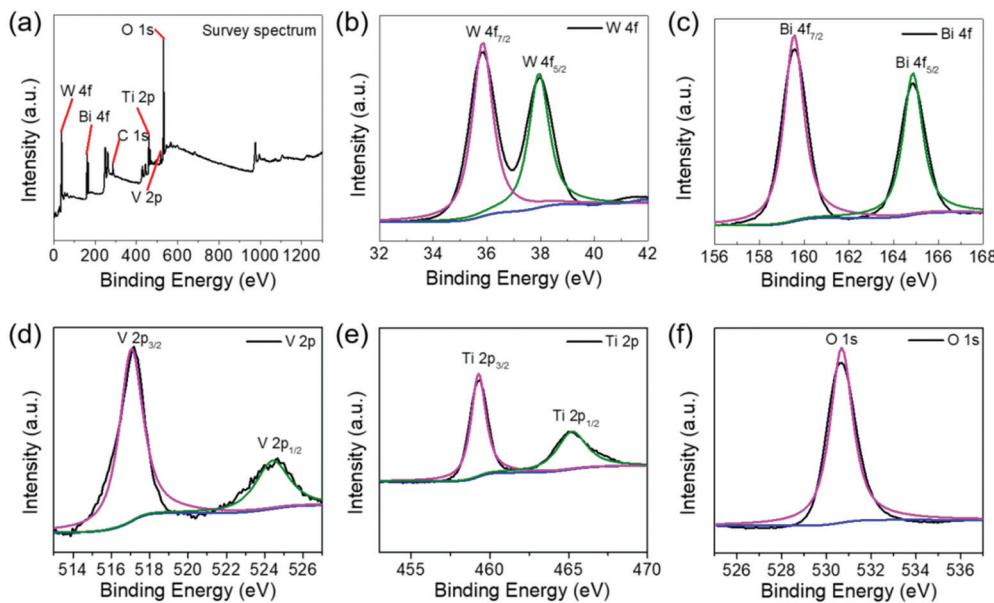


Fig. 4 XPS survey of (a) full spectra, (b) W 4f, (c) Bi 4f, (d) V 2p, (e) Ti 2p, and (f) O 1s region of $\text{WO}_3/\text{BiVO}_4/\text{TiO}_2$.

eV, shown in Fig. 4f, can be assigned to lattice oxygen (O^{2-}) and surface hydroxyl species.³⁰

We employed ultraviolet-visible (UV-vis) absorption spectroscopy to understand the light absorption characteristics. As seen from Fig. 5a, the strong light absorption within a range of 325–460 nm was revealed for pristine WO_3 electrodes, whereas $\text{WO}_3/\text{BiVO}_4$ and $\text{WO}_3/\text{BiVO}_4/\text{TiO}_2$ exhibited longer wavelength light absorption in the range of 360–500 nm, demonstrating enhanced light absorption ability in the latter. IPCE spectra *vs.* wavelength was measured with various band-pass filters in a xenon (Xe) lamp, showing a red shift in the light absorption (Fig. 5b). The band gap values were ~ 2.60 eV, 2.46 eV, and 2.44 eV, for WO_3 , $\text{WO}_3/\text{BiVO}_4$ and $\text{WO}_3/\text{BiVO}_4/\text{TiO}_2$, respectively, as shown by the plot in Fig. 5c of $(\text{IPCE} \cdot h\nu)^{1/2}$ *vs.* $h\nu$; this is in close agreement with band gap values estimated by the Tauc plot (ESI Fig. S4†) acquired from previous optical absorption spectroscopy (Fig. 5a).

Considering the absorption in the visible region, we measured photoelectrochemical performances of $\text{WO}_3/\text{BiVO}_4/\text{TiO}_2$ electrodes for water splitting and compared them with those of referenced $\text{WO}_3/\text{BiVO}_4$ and WO_3 electrodes in 0.5 M Na_2SO_4 under standard simulated sunlight illumination (1 sun) at $1.23\text{ V}_{\text{RHE}}$. Fig. 6a shows the linear sweep voltammetry (LSV) curves of the prepared photoanodes, which were recorded at room temperature under chopped light steps (10 s). The photocurrent density at $1.23\text{ V}_{\text{RHE}}$ followed the order $\text{WO}_3/\text{BiVO}_4/\text{TiO}_2$ (1.04 mA cm^{-2}) $>$ $\text{WO}_3/\text{BiVO}_4$ (0.43 mA cm^{-2}) $>$ WO_3 (0.23 mA cm^{-2}), indicating a substantial improvement in the photoelectrocatalytic performance with addition of BiVO_4 and TiO_2 layers. This ~ 2.5 times enhancement can be associated with interparticle electron transfer between integrated electrode materials and suppressed charge recombination due to the heterojunction effect.^{31,32} In addition, $\text{WO}_3/\text{BiVO}_4/\text{TiO}_2$ showed an onset potential of 500 mV *vs.* RHE, which was lower than that of WO_3 (800 mV *vs.* RHE) and $\text{WO}_3/\text{BiVO}_4$ (550 mV *vs.* RHE). The shift of the onset potential toward the negative further facilitates the electron drive from the conduction band (CB) of TiO_2 to BiVO_4 and then BiVO_4 to WO_3 .³³ This enhancement in anodic photocurrents was consistent with IPCE results (see Fig. 5b) of considerably higher values (45%) for the $\text{WO}_3/\text{BiVO}_4/\text{TiO}_2$ electrode, indicating that the photocurrent is dependent on light absorption and consistent with improved performance. To determine the flat

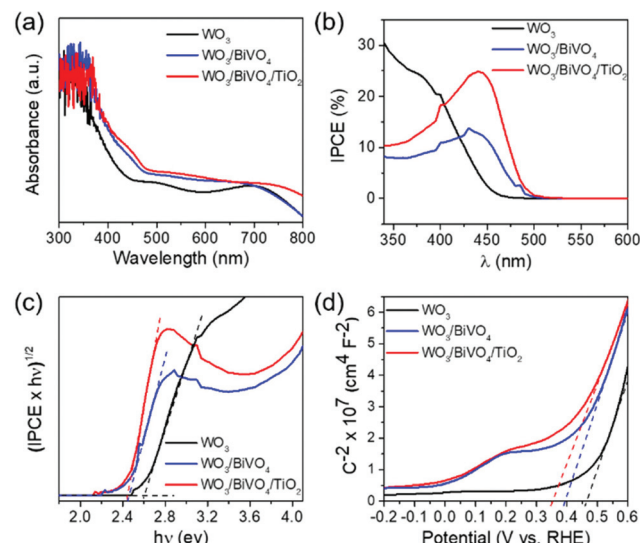


Fig. 5 Optoelectronic characterization of (a) UV-vis absorption spectra, (b) IPCE spectra, (c) $(\text{IPCE} \cdot h\nu)^{1/2}$ *vs.* $h\nu$ plots, and (d) Mott-Schottky plots of WO_3 , $\text{WO}_3/\text{BiVO}_4$, and $\text{WO}_3/\text{BiVO}_4/\text{TiO}_2$ photoelectrodes.

$\text{BiVO}_4/\text{TiO}_2$ showed an onset potential of 500 mV *vs.* RHE, which was lower than that of WO_3 (800 mV *vs.* RHE) and $\text{WO}_3/\text{BiVO}_4$ (550 mV *vs.* RHE). The shift of the onset potential toward the negative further facilitates the electron drive from the conduction band (CB) of TiO_2 to BiVO_4 and then BiVO_4 to WO_3 .³³ This enhancement in anodic photocurrents was consistent with IPCE results (see Fig. 5b) of considerably higher values (45%) for the $\text{WO}_3/\text{BiVO}_4/\text{TiO}_2$ electrode, indicating that the photocurrent is dependent on light absorption and consistent with improved performance. To determine the flat

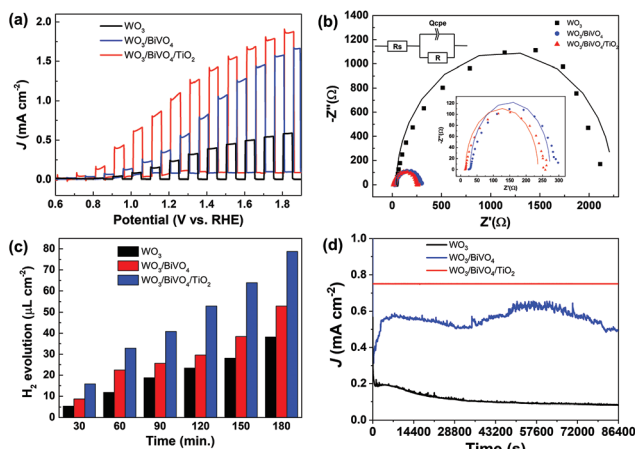


Fig. 6 Photoelectrochemical performance of WO_3 , $\text{WO}_3/\text{BiVO}_4$, and $\text{WO}_3/\text{BiVO}_4/\text{TiO}_2$ photoelectrodes: (a) Linear sweep voltammetry curves, (b) Nyquist plots and equivalent circuit, (c) plot of H_2 evolution as a function of time, and (d) chronoamperometric current density–voltage (J – T) curves.

band potentials and donor density, a Mott–Schottky analysis was performed in 0.5 M Na_2SO_4 . As seen in Fig. 5d, the electrode has a positive slope, suggesting n-type semiconductor behavior.³⁴ The flat band potential values can be estimated using eqn (4); they were 0.35 V, 0.39 V, and 0.46 V vs. RHE for the $\text{WO}_3/\text{BiVO}_4/\text{TiO}_2$, $\text{WO}_3/\text{BiVO}_4$, and WO_3 electrodes, respectively.

As a control experiment, an amorphous TiO_2 layer was coated onto our $\text{WO}_3/\text{BiVO}_4$ electrode by adopting a previously reported procedure.^{18,35} Results showed reduced photocurrent density, representing weaker interaction between host ($\text{WO}_3/\text{BiVO}_4$) and guest (amorphous- TiO_2) counterparts (Fig. S5†). This reduction in the photocurrent density of $\text{WO}_3/\text{BiVO}_4/\text{TiO}_2$ (amorphous) was presumably due to the low electric conductivity and defective amorphous TiO_2 reported previously.^{36,37} In addition, a 5-cycle coated TiO_2 electrode exhibited low photocurrent density (Fig. S6†), presumably due to the presence of high thickness and defective polycrystalline TiO_2 , as evident from previous XRD results.³⁷

To gain more insights into charge transfer kinetics at the interface of the photoanode/electrolyte, electrochemical impedance spectroscopy (EIS) was performed. Fig. 6b shows the EIS Nyquist plots of WO_3 , $\text{WO}_3/\text{BiVO}_4$, and $\text{WO}_3/\text{BiVO}_4/\text{TiO}_2$, which were fitted to the equivalent circuit (Fig. 6b) and consisted of solution resistance (R_s), charge transfer resistance (R_{ct}), and constant phase element (Q_{CPE}).³⁸ The equivalent circuit-fitted values are summarized in Table 1. It is apparent that $\text{WO}_3/\text{BiVO}_4/\text{TiO}_2$ displays a smaller R_{ct} value (228.3 Ω), when compared to WO_3 (2063 Ω) and $\text{WO}_3/\text{BiVO}_4$ (244.1 Ω). This indicates that charge transfer resistance was reduced after a coating of TiO_2 nanoparticles was applied.

These features suggest that creating a heterojunction with BiVO_4 and crystalline TiO_2 is an effective way to optimize the separation efficiency of electron–hole pairs, which would

Table 1 Fitted values of each parameter in EIS results

Parameter	WO_3	WB	WBT
R_s (Ω)	42.47	29.05	14.96
R_{ct} (Ω)	2063	244.1	228.3
Q_{CPE} (F)	42.32×10^{-6}	0.18623×10^{-3}	69.16×10^{-6}

promote overall photoelectrocatalytic performance.³⁵ Photoelectrochemical H_2 gas evolution was performed under standard sunlight irradiation (1 Sun) for a 3 h duration. The H_2 evolution rates were $78.8 \mu\text{L cm}^{-2}$ and $52.9 \mu\text{L cm}^{-2}$ for $\text{WO}_3/\text{BiVO}_4/\text{TiO}_2$ and $\text{WO}_3/\text{BiVO}_4$ photoelectrodes, respectively, at 1.23 V vs. RHE under simulated solar light (AM 1.5, 100 mW cm^{-2}); the larger HER rate represents the positive effect of crystalline TiO_2 deposition (Fig. 6c). The durability test (J – T curve) of $\text{WO}_3/\text{BiVO}_4/\text{TiO}_2$ displayed almost unchanged initial photocurrent density after 24 h of operation (Fig. 6d), whereas unmodified $\text{WO}_3/\text{BiVO}_4$ exhibited an initial drastic loss in photocurrent that the latter managed to retain after 0.5 h of operation, demonstrating robustness of ternary $\text{WO}_3/\text{BiVO}_4/\text{TiO}_2$ as a photoelectrocatalyst for water splitting. The stable photocurrent density value of $\sim 0.76 \text{ mA cm}^{-2}$ (Fig. 6d) obtained in this study is comparable to that of state-of-the-art $\text{WO}_3/\text{BiVO}_4$ photoanodes and other BiVO_4 -based photoanodes, such as $\text{WO}_3/\text{BiVO}_4$ (0.6 mA cm^{-2} at 1.23 V_{RHE}, 0.1 M Kpi),³⁹ $\text{SnO}_2/\text{WO}_3/\text{BiVO}_4$ (1.5 mA cm^{-2} at 1.23 V_{RHE}, Kpi with 0.1 M Na_2SO_3),⁴⁰ $\text{WO}_3/\text{BiVO}_4/\text{FeO}_3$ (1.1 mA cm^{-2} at 1.5 V_{RHE}, 0.5 M Na_2SO_4),¹⁴ and $\text{SnO}_2/\text{BiVO}_4/\text{Co-Pi}$ (0.8 mA cm^{-2} at 1.23 V_{RHE}, 0.1 M Kpi).⁴¹ Please see Table S1† for more details.

Guided by observations and experimental results, a plausible electron transfer mechanism of a $\text{WO}_3/\text{BiVO}_4/\text{TiO}_2$ photoelectrode is illustrated in Fig. 7. The band gap alignment was assigned on the basis of estimated optical band gap values and flat band potentials. Pristine WO_3 is a relatively weak n-type material that can possess an optical absorption onset $\sim 2.7 \text{ eV}$, while $\text{WO}_3/\text{BiVO}_4$ has strong n-type behavior due to the heterojunction effect, producing large built-in potential at the interfaces and extended light absorption over wide band gap ranges (2.4–2.7 eV). When BiVO_4 is in strong contact with WO_3 , a type II band offset can be produced that transfers electrons from the BiVO_4 CB (+0.02 V vs. RHE) to the WO_3 CB (+0.41 V vs. RHE) and facilitates electron–hole separation.⁴² Interestingly, since the CB edge potential is more negative in a $\text{WO}_3/\text{BiVO}_4/\text{TiO}_2$ heterostructure, TiO_2 would begin by inducing an electron transfer from the TiO_2 CB to the BiVO_4 CB and then inject into WO_3 electrode's CB. Thus, accumulated electrons would be injected into a current collector and migrate to the metallic cathode (Pt) electrode to participate in the hydrogen evolution reaction. We assume that introducing a thin crystalline TiO_2 overlayer would not allow hole accumulation driving forces (higher valence band potential). However, it could block surface defects that are centric to electron–hole recombination and lower the overpotential of photoelectrochemical reactions, leading to improved reaction kinetics. As a result, hole transfer going from the BiVO_4 valence band (VB) to

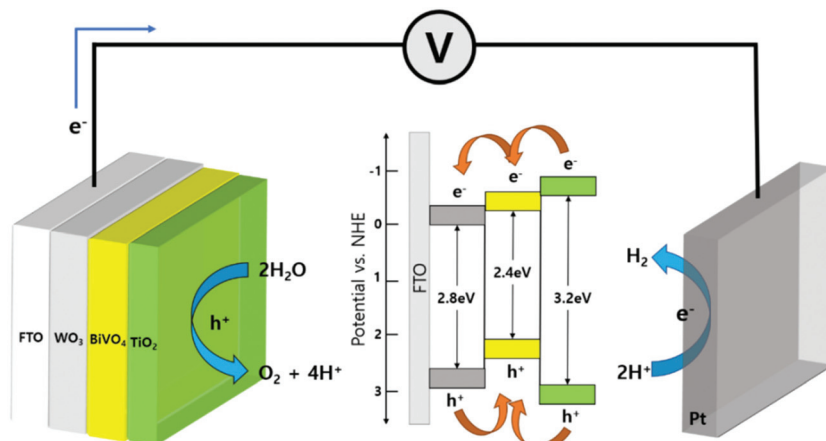


Fig. 7 Electron transfer mechanism of a $\text{WO}_3/\text{BiVO}_4/\text{TiO}_2$ photoelectrode.

the WO_3 VB would occur at the photoelectrode/electrolyte interface, leading to an oxygen evolution reaction with water molecules. In account, the as-formed $\text{WO}_3/\text{BiVO}_4/\text{TiO}_2$ photoelectrode with porous surface morphology produced from nearly vertical nanoplate-like structures provides a more accessible surface area, a type II heterojunction, and a thin crystalline TiO_2 layer, which should synergistically boost the charge-carrier separation efficiency, photostability, and overall PEC performance without the aid of any co-catalyst or sacrificial agents.

Conclusions

We demonstrated an integrated design of $\text{WO}_3/\text{BiVO}_4/\text{TiO}_2$ photoanode material by using a simple hydrothermal-spin coating strategy, which exhibited enhanced photoelectrocatalytic activity and photostability under simulated sunlight illumination. The $\text{WO}_3/\text{BiVO}_4/\text{TiO}_2$ heterostructure displayed an outstanding photocurrent density of 1.04 mA cm^{-2} at 1.23 V vs. RHE and photostability over 24 h of operation. Postmodification with crystalline (1 0 1) TiO_2 resulted in a ≈ 2.5 times improvement in PEC performance, substantially better than referenced $\text{WO}_3/\text{BiVO}_4$. This improvement in PEC performance can be attributed to fast electron transfer at the interface due to a type II band alignment, a high light harvesting ability, and excellent corrosion robustness (characterized through EIS, HR-TEM, IPCE, and chronoamperometry analysis). A thin crystalline TiO_2 overlayer was beneficial to the blocking of surface defects, increasing the surface charge-carrier separation efficacy to hypothetically behave differently from previous amorphous- TiO_2 passivation overlayers during PEC water splitting operations. This work offers new avenues for employing crystalline TiO_2 overlayer modulations when developing commercially plausible visible-light driven photocatalyst materials.

Experimental

Methods and materials

All chemicals were of reagent grade and used without further purification. Sodium tungsten dihydrate ($\text{Na}_2\text{WO}_4 \cdot 2\text{H}_2\text{O}$, $\geq 99\%$), oxalic acid ($\text{C}_2\text{H}_2\text{O}_4$, 98%), sodium sulfate (Na_2SO_4 , $\geq 99\%$), ammonium metavanadate (NH_4VO_3 , $\geq 99\%$), bismuth (m) nitrate pentahydrate ($\text{Bi}(\text{NO}_3)_3 \cdot 5\text{H}_2\text{O}$, 98%), citric acid ($\text{C}_6\text{H}_8\text{O}_7$, $\geq 99.5\%$), polyvinyl alcohol ($(\text{C}_2\text{H}_4\text{O})_x$), and titanium (iv) butoxide ($\text{Ti}(\text{OCH}_2\text{CH}_2\text{CH}_2\text{CH}_3)_4$, 97%) were bought from Sigma Aldrich. Hydrochloric acid (HCl , $35\text{--}37\%$), nitric acid (HNO_3 , 60%), and isopropyl alcohol ($\text{C}_3\text{H}_8\text{O}$, 99.5%) were purchased from Samchun Chemicals.

Synthesis of nanoplate-like WO_3

WO_3 nanostructures were fabricated on FTO coated glass substrates using a hydrothermal method. Prior to deposition, the substrates ($2 \times 4 \text{ cm}^2$) were cleaned with acetone, ethanol, and deionized (DI) water using an ultrasonicator before being dried with N_2 gas. They were then placed in a polyparaphenol (PPL)-lined reactor with their conducting sides facing downward. In typical synthesis, 0.16 g of $\text{Na}_2\text{WO}_4 \cdot 2\text{H}_2\text{O}$ was dissolved in 20 mL DI water before adding 4 mL of 3 M HCl . Next, 20 mL of 35 mM $\text{C}_2\text{H}_2\text{O}_4$ and 0.05 g of Na_2SO_4 (morphological agent) was added. The entire solution (30 mL) was then transferred into a PPL-lined autoclave and maintained at 140°C for 2 h . After the reaction, the reactor was allowed to cool naturally to room temperature. The WO_3 -coated FTO electrode was cleaned using DI water and air annealed at 500°C for 2 h .

Synthesis of $\text{WO}_3/\text{BiVO}_4$ heterojunction photoelectrodes

A BiVO_4 layer was deposited onto premade WO_3/FTO ($2 \times 2 \text{ cm}^2$) by spin coating the precursor solution at 3000 rpm for 30 s (20 cycles). In a typical synthesis, 1.17 g of NH_4VO_3 , 10 mL of HNO_3 , and 20 mL of DI water were mixed together and stirred for 30 min to dissolve the precursors. Then, 4.85 g of

Bi(NO₃)₃·5H₂O and 1.92 g of C₆H₈O₇ were added to the mixture before stirring to allow dissolution. When the solution color turned blue, 6 mL of the solution was mixed with 2 mL of (C₂H₄O)_x solution (0.4 g in 40 mL DI water) and kept under sonication for 5 min. The as-obtained films were dried at 100 °C for 5 min and air annealed at 500 °C for 30 min.

Synthesis of TiO₂ thin layers onto the WO₃/BiVO₄ heterojunction

TiO₂ precursor solution was prepared by dissolving 0.1 M Ti (OCH₂CH₂CH₂CH₃)₄ in a mixed solvent of 20 mL C₃H₈O, 0.18 g DI water, and 0.331 g HNO₃. The resultant solution was ultrasonicated for 1 h to allow complete dissolution. TiO₂ was then deposited onto the as-obtained WO₃/BiVO₄ by spin coating the above solution mixture at 3000 rpm for 40 s and annealing it at 500 °C for 1 h.

Characterization

The surface morphologies were examined by FE-SEM (JSM-6701 F, JEOL). Crystalline structures were characterized using an X-ray diffractometer (X'Pert Pro MRD, PANalytical) with a Cu-K α radiation source and a high-resolution transmission electron microscope (HR-TEM; Titan G2 ChemiSTEM, FEI Co.). XPS (NEXSA, ThermoFisher) was used to analyze the elemental composition and oxidation states of the elements present within a heterojunction. Optical absorption spectra were recorded with a UV-vis spectrophotometer (UV-1900i, Shimadzu).

PEC measurements

All PEC measurements were performed with a potentiostat (SP150, Bio-logic) under a solar simulator (LCS-100, Oriel Instruments) with a 100 W xenon arc lamp (100 mW cm⁻²). The electrolyte used was a 0.5 M Na₂SO₄ solution and the light exposed area of the photoanode was 1.5 cm². A standard three-electrode cell, consisting of silver/silver chloride (Ag/AgCl) and Pt mesh, was used as reference and counter electrodes. The as-prepared photoanodes were used as working electrodes. LSV was performed at a scan rate of 5 mV s⁻¹. IPCE (%) was measured at 1.23 V vs. RHE, using a light source and monochromator (MonoRa200, DONGWOO OPTRON) and the following equation:

$$\text{IPCE}(\%) = \frac{hc \times J_{\text{ph}}}{\lambda \times P} \times 100, \quad (1)$$

where h is the Planck constant, c is the velocity of light, J_{ph} is the photocurrent density, λ is the incident wavelength, and P is the power density of light which is measured at each wavelength.

The measured potentials were converted into the RHE using the following equations:

$$E_{\text{RHE}} = E_{\text{Ag/AgCl}} + (0.0591 \times \text{pH}) + E_{\text{Ag/AgCl}}^{\circ} \quad (2)$$

and

$$E_{\text{Ag/AgCl}} (3 \text{ M KCl}) = 0.1976 \text{ V at } 25^{\circ}\text{C}. \quad (3)$$

The Mott–Schottky plots were obtained using

$$\frac{1}{C^2} = \frac{2}{e\epsilon\epsilon_0 N_d} \left(V - V_{\text{fb}} - \frac{kT}{e} \right), \quad (4)$$

where C is the space charge layer capacitance, e is electron charge, ϵ is the dielectric constant, ϵ_0 is the vacuum permittivity, N_d is the electron donor density, V is the applied potential, V_{fb} is the flat band potential, k is the Boltzmann constant, C^{-2} indicates applied potential, and T is the temperature. The x intercept and the linear fit determine the flat band potential.

EIS measurements were performed within the frequency range of 50 kHz–100 MHz at 1.21 V vs. RHE. To examine evolved H₂ gas during the PEC process, 200 μ L of gas was taken from the sealed quartz tube system every half hour and injected into a gas chromatograph (Agilent 6850, Agilent Technologies).

Author contributions

E. Park: conceptualization, data curation, formal analysis, methodology, visualization, writing – original draft, and writing – review and editing; S. S. Patil: formal analysis, methodology, and writing – review and editing; H. Lee: formal analysis, methodology, and writing – review and editing; V. S. Kumbhar: conceptualization, supervision, writing – original draft, and writing – review and editing; K. Lee: conceptualization, supervision, writing – original draft, writing – review and editing, and funding acquisition.

Conflicts of interest

There are no conflicts to declare.

Acknowledgements

This research was supported by the National Research Foundation of Korea [grant numbers NRF-2019R1I1A3A01041454], funded by the South Korean Government particularly the Ministry of Education.

References

- 1 J. H. Kim and J. S. Lee, BiVO₄-Based heterostructured photocatalysts for solar water splitting: A review, *Energy Environ. Focus*, 2014, 3(4), 339–353.
- 2 M. G. Lee, J. S. Park and H. W. Jang, Solution-processed metal oxide thin film nanostructures for water splitting photoelectrodes: A review, *J. Korean Ceram. Soc.*, 2018, 55(3), 185–202.
- 3 B. S. Kalanoor, H. Seo and S. S. Kalanur, Recent developments in photoelectrochemical water-splitting using WO₃/BiVO₄ heterojunction photoanode: A review, *Mater. Sci. Energy Technol.*, 2018, 1(1), 49–62.

4 T. Hisatomi and K. Domen, Introductory lecture: Sunlight-driven water splitting and carbon dioxide reduction by heterogeneous semiconductor systems as key processes in artificial photosynthesis, *Faraday Discuss.*, 2017, **198**(0), 11–35.

5 F. E. Osterloh, Inorganic nanostructures for photoelectrochemical and photocatalytic water splitting, *Chem. Soc. Rev.*, 2013, **42**(6), 2294–2320.

6 V. S. Kumbhar, H. Lee, J. Lee and K. Lee, Interfacial growth of the optimal BiVO_4 nanoparticles onto self-assembled WO_3 nanoplates for efficient photoelectrochemical water splitting, *J. Colloid Interface Sci.*, 2019, **557**, 478–487.

7 F. A. Honda, Electrochemical Photolysis of Water at a Semiconductor Electrode, *Nature*, 1972, **238**, 37–38.

8 V. O. Smilyk, S. S. Fomanyuk, G. Y. Kolbasov, I. A. Rusetskyi and V. S. Vorobets, Electrodeposition, optical and photoelectrochemical properties of BiVO_4 and $\text{BiVO}_4/\text{WO}_3$ films, *Res. Chem. Intermed.*, 2019, **45**(8), 4149–4161.

9 C. Liu, Y. Yang, J. Li, S. Chen, W. Li and X. Tang, An in situ transformation approach for fabrication of $\text{BiVO}_4/\text{WO}_3$ heterojunction photoanode with high photoelectrochemical activity, *Chem. Eng. J.*, 2017, **326**, 603–611.

10 L. Xia, J. Bai, J. Li, Q. Zeng, X. Li and B. Zhou, A highly efficient $\text{BiVO}_4/\text{WO}_3/\text{W}$ heterojunction photoanode for visible-light responsive dual photoelectrode photocatalytic fuel cell, *Appl. Catal., B*, 2016, **183**, 224–230.

11 J. H. Baek, B. J. Kim, G. S. Han, S. W. Hwang, D. R. Kim, I. S. Cho and H. S. Jung, $\text{BiVO}_4/\text{WO}_3/\text{SnO}_2$ Double-heterojunction photoanode with enhanced charge separation and visible-transparency for bias-free solar water-splitting with a perovskite solar cell, *ACS Appl. Mater. Interfaces*, 2017, **9**(2), 1479–1487.

12 P. Chatchai, Y. Murakami, S.-y. Kishioka, A. Y. Nosaka and Y. Nosaka, Efficient photocatalytic activity of water oxidation over $\text{WO}_3/\text{BiVO}_4$ composite under visible light irradiation, *Electrochim. Acta*, 2009, **54**(3), 1147–1152.

13 Y. Park, K. J. McDonald and K.-S. Choi, Progress in bismuth vanadate photoanodes for use in solar water oxidation, *Chem. Soc. Rev.*, 2013, **42**(6), 2321–2337.

14 S. Khoomortezaei, H. Abdizadeh and M. R. Golobostanfar, Triple layer heterojunction $\text{WO}_3/\text{BiVO}_4/\text{BiFeO}_3$ porous photoanode for efficient photoelectrochemical water splitting, *ACS Appl. Energy Mater.*, 2019, **2**(9), 6428–6439.

15 Z. Zhang, B. Chen, M. Baek and K. Yong, Multichannel charge transport of a $\text{BiVO}_4/(\text{RGO}/\text{WO}_3)/\text{W18O49}$ three-storey anode for greatly enhanced photoelectrochemical efficiency, *ACS Appl. Mater. Interfaces*, 2018, **10**(7), 6218–6227.

16 I. Grigioni, A. Corti, M. V. Dozzi and E. Selli, Photoactivity and Stability of $\text{WO}_3/\text{BiVO}_4$ Photoanodes: Effects of the contact electrolyte and of Ni/Fe oxyhydroxide protection, *J. Phys. Chem. C*, 2018, **122**(25), 13969–13978.

17 X. Zhang, X. Wang, D. Wang and J. Ye, Conformal BiVO_4 -Layer/ WO_3 -Nanoplate-array heterojunction photoanode modified with cobalt phosphate cocatalyst for significantly enhanced photoelectrochemical performances, *ACS Appl. Mater. Interfaces*, 2019, **11**(6), 5623–5631.

18 S. S. Kalanur, I.-H. Yoo, J. Park and H. Seo, Insights into the electronic bands of $\text{WO}_3/\text{BiVO}_4/\text{TiO}_2$, revealing high solar water splitting efficiency, *J. Mater. Chem. A*, 2017, **5**(4), 1455–1461.

19 T. Zhang, J. Su and L. Guo, Morphology engineering of $\text{WO}_3/\text{BiVO}_4$ heterojunctions for efficient photocatalytic water oxidation, *CrystEngComm*, 2016, **18**(46), 8961–8970.

20 Y. Zhang, D. Zhang, X. Xu and B. Zhang, Morphology control and photocatalytic characterization of WO_3 nanofiber bundles, *Chin. Chem. Lett.*, 2018, **29**(9), 1350–1354.

21 C. Wang, X. Li, C. Feng, Y. Sun and G. Lu, Nanosheets assembled hierarchical flower-like WO_3 nanostructures: Synthesis, characterization, and their gas sensing properties, *Sens. Actuators, B*, 2015, **210**, 75–81.

22 J. Yin, S. Huang, Z. Jian, Z. Wang and Y. Zhang, Fabrication of heterojunction $\text{SnO}_2/\text{BiVO}_4$ composites having enhanced visible light photocatalytic activity, *Mater. Sci. Semicond. Process.*, 2015, **34**, 198–204.

23 Z. Jiao, H. Yu, X. Wang and Y. Bi, Ultrathin BiVO_4 nanobelts: controllable synthesis and improved photocatalytic oxidation of water, *RSC Adv.*, 2016, **6**(77), 73136–73139.

24 F. Bella, A. B. Muñoz-García, G. Meligrana, A. Lamberti, M. Destro, M. Pavone and C. Gerbaldi, Unveiling the controversial mechanism of reversible Na storage in TiO_2 nanotube arrays: Amorphous versus anatase TiO_2 , *Nano Res.*, 2017, **10**(8), 2891–2903.

25 M. Tahir, B. Tahir and N. A. S. Amin, Gold-nanoparticle-modified TiO_2 nanowires for plasmon-enhanced photocatalytic CO_2 reduction with H_2 under visible light irradiation, *Appl. Surf. Sci.*, 2015, **356**, 1289–1299.

26 D. a. e. Nagy, Effect of the morphology and phases of WO_3 nanocrystals on their photocatalytic efficiency, *R. Soc. Chem.*, 2016, **6**, 33743–33754.

27 Z. Ma, K. Song, L. Wang, F. Gao, B. Tang, H. Hou and W. Yang, $\text{WO}_3/\text{BiVO}_4$ Type-II Heterojunction arrays decorated with oxygen-deficient ZnO passivation layer: A highly efficient and stable photoanode, *ACS Appl. Mater. Interfaces*, 2019, **11**(1), 889–897.

28 P. Guan, *In situ* anchoring Ag through organic polymer for configuring efficient plasmonic BiVO_4 photoanode, *Chem. Eng. J.*, 2019, **358**, 658–665.

29 L. Shi, C. Xu, X. Sun, H. Zhang, Z. Liu, X. Qu and F. Du, Facile fabrication of hierarchical $\text{BiVO}_4/\text{TiO}_2$ heterostructures for enhanced photocatalytic activities under visible-light irradiation, *J. Mater. Sci.*, 2018, **53**(16), 11329–11342.

30 J. Z. Yin, S. B. Huang, Z. C. Jian, M. L. Pan, Y. Q. Zhang, Z. B. Fei and X. R. Xu, Enhancement of the visible light photocatalytic activity of heterojunction $\text{In}_2\text{O}_3/\text{BiVO}_4$ composites, *Appl. Phys. A*, 2015, **120**(4), 1529–1535.

31 S. S. Gujral, A. N. Simonov, M. Higashi, R. Abe and L. Spiccia, Optimization of titania post-necking treatment of TaON photoanodes to enhance water-oxidation activity under visible-light irradiation, *ChemElectroChem*, 2015, **2**(9), 1270–1278.

32 N. Hirayama, H. Nakata, H. Wakayama, S. Nishioka, T. Kanazawa, R. Kamata, Y. Ebato, K. Kato, H. Kumagai, A. Yamakata, K. Oka and K. Maeda, Solar-driven photoelectrochemical water oxidation over an n-type lead-titanium oxyfluoride anode, *J. Am. Chem. Soc.*, 2019, **141**(43), 17158–17165.

33 A. P. Singh, N. Kodan, B. R. Mehta, A. Held, L. Mayrhofer and M. Moseler, Band edge engineering in $\text{BiVO}_4/\text{TiO}_2$ heterostructure: Enhanced photoelectrochemical performance through improved charge transfer, *ACS Catal.*, 2016, **6**(8), 5311–5318.

34 C. Liu, J. Su and L. Guo, Comparison of sandwich and fingers-crossing type $\text{WO}_3/\text{BiVO}_4$ multilayer heterojunctions for photoelectrochemical water oxidation, *RSC Adv.*, 2016, **6**(33), 27557–27565.

35 D. Eisenberg, H. S. Ahn and A. J. Bard, Enhanced photoelectrochemical water oxidation on bismuth vanadate by electrodeposition of amorphous titanium dioxide, *J. Am. Chem. Soc.*, 2014, **136**(40), 14011–14014.

36 N. Wu, J. Wang, D. N. Tafen, H. Wang, J.-G. Zheng, J. P. Lewis, X. Liu, S. S. Leonard and A. Manivannan, Shape-enhanced photocatalytic activity of single-crystalline anatase TiO_2 (101) nanobelts, *J. Am. Chem. Soc.*, 2010, **132**(19), 6679–6685.

37 U. Shaislamov and B. L. Yang, CdS-sensitized single-crystalline TiO_2 nanorods and polycrystalline nanotubes for solar hydrogen generation, *J. Mater. Res.*, 2013, **28**(3), 418–423.

38 D. Hongxing, L. Qiuping and H. Yuehui, Preparation of nanoporous $\text{BiVO}_4/\text{TiO}_2/\text{Ti}$ film through electrodeposition for photoelectrochemical water splitting, *R. Soc. Open Sci.*, 2018, **5**(9), 180728.

39 D. Coelho, J. Gaudêncio, S. A. Carminati, F. W. P. Ribeiro, A. F. Nogueira and L. H. Mascaro, Bi electrodeposition on WO_3 photoanode to improve the photoactivity of the $\text{WO}_3/\text{BiVO}_4$ heterostructure to water splitting, *Chem. Eng. J.*, 2020, **399**, 125836.

40 S. S. M. Bhat, S. A. Lee, J. M. Suh, S.-P. Hong and H. W. Jang, Triple planar heterojunction of $\text{SnO}_2/\text{WO}_3/\text{BiVO}_4$ with enhanced photoelectrochemical performance under front illumination, *Appl. Sci.*, 2018, **8**(10), 1765.

41 J. Liu, J. Li, M. Shao and M. Wei, Directed synthesis of $\text{SnO}_2@\text{BiVO}_4/\text{Co-Pt}$ photoanode for highly efficient photoelectrochemical water splitting and urea oxidation, *J. Mater. Chem. A*, 2019, **7**(11), 6327–6336.

42 I. Grigioni, K. G. Stamplecoskie, E. Selli and P. V. Kamat, Dynamics of photogenerated charge carriers in $\text{WO}_3/\text{BiVO}_4$ heterojunction photoanodes, *J. Phys. Chem. C*, 2015, **119**(36), 20792–20800.